Heuristic model for the growth and coupling of nonlinear processes in droplets

Ali Serpengüzel, Gang Chen, and Richard K. Chang

Department of Applied Physics and Center for Laser Diagnostics, Yale University, New Haven, Connecticut 06520

Wen-Feng Hsieh

Institute of Electro-Optical Engineering, National Chiao-Tung University, Hsinchu, Taiwan, China

Received September 4, 1991; revised manuscript received December 23, 1991

Standard one-dimensional nonlinear-wave equations are modified to accommodate the growth and coupling of nonlinear waves in droplets. The propagation direction of the nonlinear waves along the length of an optical cell is changed so that it is along the droplet rim. The model includes radiation losses because of nonzero absorption, leakage from the droplet, and depletion in generating other nonlinear waves. For multimode-laser input, the growth and decay of the first- through fourth-order Stokes stimulated Raman scattering (SRS) are calculated as a function of the phase matching of the four-wave mixing process and the model-dependent Raman gain coefficient. The Raman gain coefficient determines the delay time of the first-order SRS, while the phase matching determines the correlated temporal profiles of the multiorder SRS. Both the Raman gain and the phase matching are found to be enhanced in the droplet. The spatial distribution of the internal input-laser intensity is calculated by using the Lorenz–Mie formalism. The temporal profile of the input-laser intensity used in the calculations is identical to the experimentally observed laser time profile. The delay time and the correlated growth and decay of nonlinear waves resulting from the numerical simulation compare favorably with those of the experimental observations. Similar calculations are made for single-mode-laser input for which the stimulated Brillouin scattering (SBS) achieves its threshold before the SRS does and subsequently pumps the SRS.

1. INTRODUCTION

In a liquid cell, the input pump and the resultant nonlinear beams are generally assumed to be one dimensional and spatially overlapping along the copropagation direction. In a mirrorless optical cell, the growth, decay, and coupling of the nonlinear processes, such as stimulated Raman scattering (SRS) and stimulated Brillouin scattering (SBS), need not include feedback. For a liquid droplet, because of the spherical liquid–air interface, three electromagnetic and quantum-electrodynamic (QED) effects can occur. First, the internal-input intensity I_{input} (at the wavelength λ_{input}) is usually concentrated (with $\approx 10^2 \times$ enhancement) in two small regions along the principal diameter just within the droplet shadow and the illuminated faces (see Fig. 1). Second, the generated nonlinear waves circulate around the droplet rim because the droplet acts as an optical cavity (with quality factor $Q \approx 10^6$) for specific wavelengths that satisfy the morphology-dependent resonances (MDR's) of the droplet cavity and are within the spontaneous Raman (or Brillouin) gain profile. MDR's are usually treated as standing waves[1] that can be decomposed into two counterpropagating waves traveling around the droplet rim. Third, the spontaneous Raman (or Brillouin) cross sections of molecules in the droplets can be larger than those in an optical cell because of the modified density of final states for the spontaneous Raman (or Brillouin) transition rates.[2] In the droplet, the final states are the droplet-cavity modes, which are described by MDR's, while for the optical cell the final states are the continuum modes of an infinite system.[3]

When a Q-switched Nd:YAG laser is operated in its single-mode option, the linewidth of the green second-harmonic output ($\lambda_{\text{input}} = 532$ nm) is less than that of the SBS. For most liquid droplets, the SBS threshold is $\approx 3 \times$ lower than the SRS threshold.[4] A time-resolved study revealed a time delay between the SBS and the input-laser pulses as well as a correlated growth and decay of the SBS and the SRS pulses. The conclusion is drawn that the input-laser radiation pumps the SBS wave and the resultant SBS wave then pumps the SRS wave and becomes depleted.

When the Q-switched Nd:YAG laser is operated in the multimode option, the green second-harmonic output ($\lambda_{\text{input}} = 532$ nm) has a linewidth greater than the spontaneous Brillouin linewidth. Consequently, for most liquid droplets, the SBS threshold is higher than the SRS threshold, and the SRS is directly pumped by the input-laser beam. Several experiments using a multimode laser[5–7] dealt with the delay time between the various-order Stokes SRS and the input-laser pulses. The correlated growth and decay of the jth and $(j + 1)$th-order Stokes SRS waves were also noted.[7]

To our knowledge, there does not exist a set of nonlinear-wave equations that can describe the experimental observations of delay times and correlated growths and decays among the SBS and the various-order Stokes SRS waves in single droplets. In this paper the standard one-dimensional coupled nonlinear-wave equations for SBS and SRS in an optical cell[8] are modified to describe the growth and coupling of nonlinear waves circulating around the droplet rim. In our heuristic model the input

0740-3224/92/060871-13$05.00

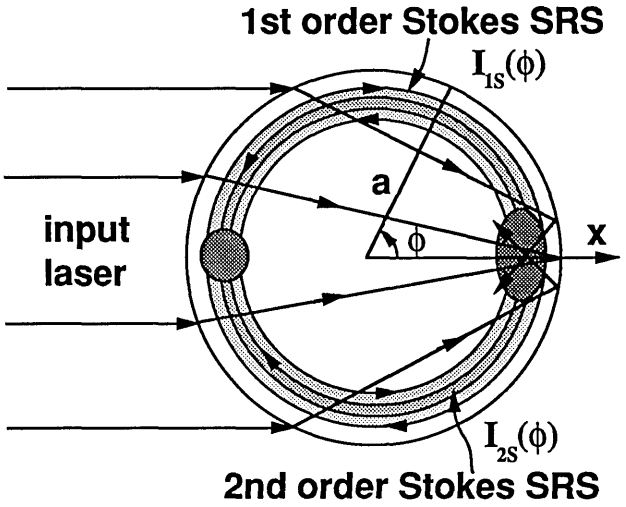

Fig. 1. Schematic of the spatial distribution of the intensity (shaded areas) and the rays of the input-laser first- and second-order Stokes SRS waves in the droplet equatorial plane. The intensity maximum of the input-laser beam is concentrated on the shadow side of the droplet at $\phi = 0°$. The generated first- and second-order Stokes SRS waves are on MDR's, which are represented as two counterpropagating traveling waves or standing waves around the droplet rim. The droplet has radius **a**, and ϕ is the azimuthal angle.

laser is assumed to be a plane wave, and the internal input-intensity distribution is calculated by using Lorenz–Mie theory. The time dependence of the input intensity used in our calculation is that of the experimentally observed time profile. The internal-input intensity used in our model is assumed to be undepleted by the nonlinear waves. Furthermore, in the model the SBS (or first-order Stokes SRS) starts from the spontaneous Brillouin (or Raman) noise. The higher-order Stokes SRS starts from both the spontaneous Raman noise and the parametric noise associated with the four-wave mixing (FWM) among the multi-order Stokes SRS waves. For each round trip around the droplet rim, the Brillouin (or Raman) wave experiences gain as it traverses the two internal high-intensity input-pump regions, which are localized just within the droplet shadow and the illuminated faces and which are along the droplet's principal diameter (parallel to the incident laser-beam direction). Because of the QED effect on the spontaneous and stimulated transition rates,[3,9] the model-dependent Brillouin and Raman gain coefficients are adjustable parameters that can exceed the values normally used for the liquid cell. During each round trip, the nonlinear wave experiences losses because of linear absorption, radiation leakage[10] commensurate with the Q of the MDR and intensity depletion resulting from nonlinear coupling to other internal waves. The delay times for SBS and SRS are deduced from the number of round trips needed to achieve a total gain[8] of $\approx$exp(30). With slightly enhanced values for the model-dependent Raman gain coefficient, the calculated delay times between the nonlinear waves (e.g., SBS and various-order Stokes SRS) and the laser pulse agree with the experimentally observed delay times. In addition, with enhanced phase-matching values the numerical simulation of the temporal behavior of the nonlinear waves also compares favorably with the experimental results, which exhibited correlated decay of the nonlinear pump waves and the growth of the resultant waves, e.g., the decay of the SBS and the growth of the first-order Stokes SRS as well as the decay of the jth-order Stokes SRS and the growth of the $(j + 1)$th-order Stokes SRS.

2. INTERNAL INTENSITY DISTRIBUTION IN A DROPLET

A. Spatial Distribution

The z axis is designated by the droplet-falling direction (along the vertical axis in the laboratory frame), and the x axis is designated by the input-laser-beam direction (along a horizontal axis in the laboratory frame). In the experiment the SBS and SRS signals are collected along the y axis. I_{input} (at frequency $\nu_{\text{input}} = \lambda_{\text{input}}^{-1}$) is assumed to be a plane wave, and the internal-intensity distribution $I_{\text{input}}(r, \theta, \phi)$ is calculated as a function of the radial distance r, the polar angle θ, and the azimuthal angle ϕ by using the Lorenz–Mie formalism.[1,11,12] The internal-field calculations are purposely selected so that ν_{input} is not on a MDR because, in all the experiments[5–7] that measure the delay times and correlated growth and decay characteristics, the droplet radius is not deliberately adjusted so that the input-laser radiation (at a fixed wavelength λ_{input}) is on a specific MDR (i.e., on an input resonance). Because ν_{input} is not on a MDR, possible self-focusing of the input-laser intensity is not included in the model. However, the SBS and all orders of Stokes SRS waves are on MDR's (i.e., on an output resonance) because the growth of these waves occurs only if the droplet acts as an optical cavity with high Q (e.g., in excess of 10^6). When the input radiation is

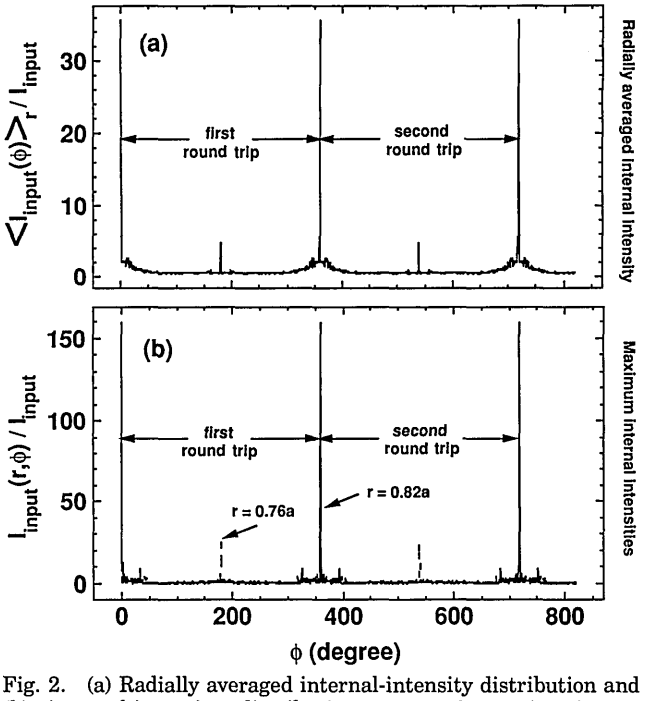

Fig. 2. (a) Radially averaged internal-intensity distribution and (b) internal-intensity distribution at $r = 0.82\mathbf{a}$ (continuous curve) and at $r = 0.76\mathbf{a}$ (dashed curve) of the input wave $I_{\text{input}}(\phi)$ as a function of the azimuthal angle ϕ in the droplet equatorial plane. The droplet shadow face is located at $\phi = 0° + n360°$, and the droplet illuminated face is located at $\phi = 180° + n360°$, where n is an integer. The range of ϕ shown is from $\phi = 0°$ to $\phi = 800°$. The first round trip around the droplet rim is from $\phi = 0°$ to $\phi = 360°$, and the second round trip is from $\phi = 360°$ to $\phi = 720°$.

not on an input resonance, $I_{\text{input}}(r, \phi)$ is highly localized and intense at $\phi \approx 0°$ and $\phi \approx 180°$ and is more uniformly distributed and relatively weak around the droplet rim for other ϕ values in the droplet equatorial plane ($\theta = 90°$; see Figs. 1 and 2).[13]

The internal-field distributions of the nonlinear waves that are on an output resonance are assumed to acquire the internal-field distributions of the MDR's. For MDR's with high Q's, the internal-field intensity of MDR's is radially confined between $\mathbf{a}/m(\nu)$ and $\mathbf{a}$ [where $\mathbf{a}$ is the droplet radius and $m(\nu)$ is the ratio of the index of refraction of the liquid to that of the surrounding air at an optical frequency ν]. The peak of the internal intensity in the radial direction is dependent on the radial-mode order l of the MDR.[11] In the equatorial plane ($\theta = 90°$), the MDR's, which are usually considered as standing waves, have $2n$ intensity peaks at $0° \leq \phi \leq 360°$, where n is the MDR mode number. However, the standing-wave nature of the MDR can be decomposed as two counterpropagating traveling waves around the droplet rim. Recognizing that MDR's can be decomposed into two traveling waves is central to the modification of the standard one-dimensional nonlinear-wave equations to describe the growth and decay of nonlinear waves in droplets.

For the nonlinear waves to experience gain from $I_{\text{input}}(r, \theta, \phi)$, there must be some spatial overlap between the internal-intensity distribution of the MDR and that of $I_{\text{input}}(r, \theta, \phi)$. Such spatial overlap is largest for MDR's that are localized in the equatorial plane and in all equivalent planes that are axisymmetric with respect to the x axis. Consequently, when viewed along the y axis and at an input intensity just above the SBS and SRS thresholds, the detected nonlinear waves are associated with those waves that propagate around the equator in the $\pm\phi$ directions and are in resonance with MDR's that have the azimuthal-mode number m equal to the mode number n ($m = \pm n$).[11,12] Experimentally, when viewed from the y axis and when I_{input} just exceeds the SBS (or SRS) threshold, the SBS (or the SRS) appears as two small green (or red) dots[4] located on the equator at $x = \pm\mathbf{a}$. At higher I_{input}, the SBS (or the SRS) appears as two green (or red) arcs[4] centered on the equator at $x = \pm\mathbf{a}$ and extending toward the two poles at $z = \pm\mathbf{a}$. The detected radiation from the arc is associated with the nonlinear waves that are in resonance with MDR's that have $|m| < n$. For simplicity, we consider in our model only those SBS and SRS waves that circulate around the equator (i.e., with polar angle $\theta = 90°$, where the MDR has $m = \pm n$).

The nonlinear wave, as it propagates around the equator in the $\pm\phi$ directions, experiences a spatially nonuniform gain because $I_{\text{input}}(r, \phi)$ is spatially nonuniform (see Figs. 1 and 2). Furthermore, gain occurs where there is radial overlap between $I_{\text{input}}(r, \phi)$ and the nonlinear wave, which, being on a MDR, is radially confined within $\mathbf{a}/m(\nu) < r < \mathbf{a}$. The radial confinement of the MDR's in the $\mathbf{a}/m(\nu) < r < \mathbf{a}$ region is dependent on their l values. Because we do not know the l value of the MDR that is providing the feedback for the nonlinear wave, in our simulations we use a radially averaged internal-input intensity that is integrated along the r direction in the equatorial plane ($\theta = 90°$) and is dependent only on ϕ:

$$\langle I_{\text{input}}(\phi)\rangle_r = \frac{m(\nu)}{\mathbf{a}[m(\nu) - 1]} \int_{\mathbf{a}/m(\nu)}^{\mathbf{a}} I_{\text{input}}(r, \phi)\mathrm{d}r. \quad (1)$$

Here the Lorenz–Mie formalism is used to calculate $I_{\text{input}}(r, \phi)$ for a droplet with $\mathbf{a} = 40$ μm and $m(\nu) = 1.33$. Figure 2(a) displays the radially averaged internal-input intensity $\langle I_{\text{input}}(\phi)\rangle_r$ [see Eq. (1)] as a function of ϕ, where $\phi = 0°$ is along the x axis and at the shadow face and $\phi = 180°$ is along the $-x$ axis and at the illuminated face. Figure 2(b) displays $I_{\text{input}}(r, \phi)$ as a function of ϕ at $r = 0.82\mathbf{a}$ and $r = 0.76\mathbf{a}$. At $r = 0.82\mathbf{a}$ the shadow face of the droplet has an internal-input intensity maximum. At $r = 0.76\mathbf{a}$ the illuminated face of the droplet has an internal-input intensity maximum.

B. Temporal Distribution

The observed temporal pulse shape of the input-laser beam $I_{\text{input}}(t)$ is related to the time-averaged $\langle I_{\text{input}}\rangle_t$ as follows:

$$\langle I_{\text{input}}\rangle_t = \frac{1}{\tau_{\text{input}}} \int_0^\infty I_{\text{input}}(t)\mathrm{d}t, \quad (2)$$

where τ_{input} is the FWHM of the temporal pulse profile of $I_{\text{input}}(t)$. The normalized temporal profile of the input-laser pulse $T_{\text{input}}(t)$ is defined as follows:

$$T_{\text{input}}(t) = \frac{I_{\text{input}}(t)}{\langle I_{\text{input}}\rangle_t}. \quad (3)$$

Consequently, the internal-intensity distribution in the equatorial plane as a function of the azimuthal angle and time $I_{\text{input}}(\phi, t)$ can be expressed as follows:

$$I_{\text{input}}(\phi, t) = \langle I_{\text{input}}(\phi)\rangle_r T_{\text{input}}(t). \quad (4)$$

In our numerical simulation, we first consider the growth and decay of the nonlinear waves with $T_{\text{input}}(t)$ set equal to a flattop function with $\tau_{\text{input}} = 7$ ns. Subsequently, the experimentally determined temporal behavior of the input pulse $T_{\text{input}}(t)$ is used in our calculation of the time behavior of the nonlinear waves.

3. WAVE EQUATIONS FOR SRS WITH A MULTIMODE PUMP

When the output intensity from the multimode laser is low, the SBS threshold is not reached. When viewed along the y axis, the SRS appears as two red dots located in the equatorial plane at $x = \pm\mathbf{a}$. Thus, in our heuristic model, the detected SRS waves are assumed to be associated with the nonlinear waves that are confined to the equatorial plane and circulating in the $\pm\phi$ directions. In order to describe the growth and decay of multiorder Stokes SRS in a droplet, we modified the standard coupled one-dimensional nonlinear-wave equations for the generation of multiorder Stokes SRS in an optical cell.[14] The incremental length $\mathrm{d}z$ of an optical cell is transformed to the incremental arc at the droplet rim $\mathbf{a}\,\mathrm{d}\phi$. The distance z from the front of the optical cell ($z = 0$) is transformed to an arc length $\mathbf{a}\phi$ starting from $\phi = 0°$, where $I_{\text{input}}(r, \phi)$ has a maximum. The total number of round trips around the droplet rim is equal to $\phi/360°$.

A. Nonlinear-Optical Wave Equations

In our model the coupled nonlinear-wave equations for the growth and decay of the first- and second-order Stokes SRS in a droplet are as follows:

Table 1. Parameters for the Multimode Laser Pumping SRS

Parameter	Value	Reference
Raman gain coefficient of nitrate ion	$g_S = 0.15$ cm/GW	16
Absorption loss (at ν_{1S})	$\alpha_{1S} = 0.049$ m^{-1}	17
Absorption loss (at ν_{2S})	$\alpha_{2S} = 0.23$ m^{-1}	17
Absorption loss (at ν_{3S})	$\alpha_{3S} = 0.29$ m^{-1}	17
Absorption loss (at ν_{4S})	$\alpha_{4S} = 0.43$ m^{-1}	17
Q factor of MDR's	$Q = 10^6$	18
Leakage loss (at various Stokes ν_{jS})	$L_{jS} = 2\pi\nu_{jS}m(\nu_{jS})/Q$ m^{-1}	18
Raman shift for nitrate ion	$\nu_{\text{vib}} = 1050$ cm^{-1}	7
Input-laser frequency	$\nu_{\text{input}} = 18\,797$ cm^{-1}	7
Time-averaged input-laser intensity	$\langle I_{\text{input}}\rangle_t = 0.8$ GW/cm^2	7
Droplet radius	$\mathbf{a} = 40$ μm	7
Refractive index of water	$m(\nu) = 1.33$	17
Wave-vector mismatch for water	$\Delta k = 10^3\pi$ m^{-1}	7

$$\frac{dE_{1S}}{\mathbf{a}d\phi} = \left[\frac{g_S}{2}(I_{\text{input}} - I_{2S}) - \frac{\alpha_{1S}}{2} - \frac{L_{1S}}{2}\right]E_{1S} - \frac{g_S}{2}E_{\text{input}}E_{1S}^{*}E_{2S}\exp(i\Delta k_{2S}\mathbf{a}\phi) - \sum_{j=3}^{j_{\text{final}}}\frac{g_S}{2}E_{\text{input}}E_{(j-1)S}^{*}E_{jS}\exp(i\Delta k_{jS}\mathbf{a}\phi), \quad (5a)$$

$$\frac{dE_{2S}}{\mathbf{a}d\phi} = \left[\frac{g_S}{2}\frac{\nu_{2S}}{\nu_{1S}}(I_{1S} - I_{3S}) - \frac{\alpha_{2S}}{2} - \frac{L_{2S}}{2}\right]E_{2S} + \frac{g_S}{2}\frac{\nu_{2S}}{\nu_{1S}}E_{\text{input}}^{*}E_{1S}E_{1S}\exp(i\Delta k_{2S}\mathbf{a}\phi) - \sum_{j'=3}^{j_{\text{final}}}\frac{g_S}{2}\frac{\nu_{2S}}{\nu_{1S}}E_{\text{input}}E_{(j'-2)S}^{*}E_{j'S}\exp(i\Delta k_{j'S}\mathbf{a}\phi). \quad (5b)$$

The nonlinear-wave equations for third- and higher-order Stokes SRS are similar to that for the second-order Stokes SRS [see Eq. (5b)].

The following notations are used in Eqs. (5a) and (5b): E_{input}, E_{1S}, E_{2S}, E_{3S}, and E_{jS} are the internal electric fields of the input laser first-, second-, third-, and jth-order Stokes SRS, respectively; I_{input}, I_{1S}, I_{2S}, and I_{3S} are the internal intensity of the input laser first-, second-, and third-order Stokes SRS, respectively; $\nu_{1S} = \nu_{\text{input}} - \nu_{\text{vib}}$ and $\nu_{2S} = \nu_{\text{input}} - 2\nu_{\text{vib}}$ are the frequencies of the first- and second-order Stokes SRS, respectively, where ν_{vib} is the vibrational frequency of the Raman mode (usually the vibrational mode with the largest spontaneous Raman cross section); g_S is the Raman gain coefficient for the first- and higher-order Stokes SRS; α_{1S} and α_{2S} are the absorption losses for the first- and second-order Stokes SRS, respectively; L_{1S} and L_{2S} are the cavity-radiation leakage losses for the first- and second-order Stokes SRS, respectively; subscripts j and j' are integers that designate the order of the Stokes SRS; j_{final} is the highest-order Stokes SRS included in the calculations; $\Delta k_{2S} = (k_{2S} + k_{\text{input}} - 2k_{1S})$ is the wave-vector mismatch among the internal wave vectors of the second-order SRS (k_{2S}), input laser (k_{input}), and two first-order Stokes SRS ($2k_{1S}$); $\Delta k_{jS} = [k_{jS} + k_{\text{input}} - k_{1S} - k_{(j-1)S}]$ is the wave-vector mismatch among the wave vectors of the jth-order Stokes SRS (k_{jS}), the input laser (k_{input}), the first-order Stokes SRS (k_{1S}), and the $(j-1)$th-order Stokes SRS $[k_{(j-1)S}]$; and $\Delta k_{j'S} = [k_{j'S} + k_{\text{input}} - k_{2S} - k_{(j'-2)S}]$ is the wave-vector mismatch among the wave vectors of the j'th-order Stokes SRS ($k_{j'S}$), the input laser (k_{input}), the second-order Stokes SRS (k_{2S}), and the $(j'-2)$th-order Stokes SRS $[k_{(j'-2)S}]$.

The first term on the right-hand side of Eq. (5a) corresponds to the Raman gain provided by I_{input} (assumed to be undepleted), the depletion caused by generating I_{2S}, and the losses because of absorption and leakage from the droplet. Initially, when $\mathbf{a}\phi = 0$, the source of E_{1S} is the spontaneous Raman noise I_{o1S} created by I_{input} ($\phi = 0°$). The FWM process with the second-order Stokes SRS is responsible for the depletion of I_{1S} and is described by the second term on the right-hand side of Eq. (5a). The third term on the right-hand side of Eq. (5a) describes FWM processes that include higher orders than the second-order Stokes SRS.

For the growth and decay of the second-order Stokes SRS, E_{2S} arises initially both from the spontaneous Raman noise I_{o2S} (at ν_{2S}) generated by I_{1S} and from the FWM process [the second term on the right-hand side of Eq. (5b)]. The initial source of E_{2S} generated by the FWM process is commonly referred to as the parametric noise. For the jth-order Stokes SRS, there are also two initial sources of E_{jS}, one from the spontaneous Raman process and another from the FWM process. In our calculation the coupled differential equations [similar to Eqs. (5a) and (5b)] include and extend to E_{3S} and E_{4S}. The growth and coupling of E_{5S} and higher-order Stokes SRS are neglected in our model.

In the droplet equatorial plane ($\phi = 90°$), the internal input-laser intensity has a radially averaged ϕ distribution $\langle I_{\text{input}}(\phi)\rangle_r$ [see Fig. 2(a)] and a normalized time dependence $T_{\text{input}}(t)$. The SRS waves are assumed to circulate along the $\pm\phi$ directions. For the first round trip around the droplet rim we numerically integrate Eq. (5), for four orders of Stokes SRS, as a function of ϕ starting from $\phi = 0°$ and ending at $\phi = 360°$. During the second round trip around the droplet rim we integrate Eq. (5) from $\phi = 360°$ to $\phi = 720°$. For each round trip the stimulated Raman waves experience gain, absorption, and cavity-leakage losses, and intensity depletion resulting from generating and pumping higher-order Stokes SRS. For the first round trip the spontaneous Raman noise is assumed to be $I_{o1S} = 10^{-12} \times I_{\text{input}}$ ($\phi = 0, t$) in order to be consistent with the optical-cell calculations, which also assume[15] that $I_{o1S} = 10^{-12} \times I_{\text{input}}(t)$. In our droplet calculation the value of I_{1S} reached at the end of each round trip

is then used as the starting value of the next round trip, thus simulating the feedback provided by the droplet.

Table 1 lists the values of all the parameters used in Eq. (5) for all four orders of Stokes SRS from droplets irradiated with a multimode-laser beam. The cavity-leakage loss constant L_{jS} for the jth-order Stokes SRS is related to the MDR Q (assumed to be $Q = 10^6$) as follows:

$$L_{jS} = \frac{2\pi\nu_{jS} m(\nu_{jS})}{Q}. \tag{6}$$

In Eq. (5) the same L_{jS} value is assumed for all the jth-order Stokes SRS.

B. Enhancement of the Raman Gain

Because of the QED effect,[3,9] the actual Raman gain g_S can be larger than that deduced from the measurement of spontaneous Raman intensity and linewidth $\Delta\nu_S$. In the strong coupling regime,[3] several MDR's can exist within $\Delta\nu_S$ because $\Delta\nu_S = 13$ cm^{-1} for the nitrate ion is wider than the MDR linewidth $\Delta\nu_c = \nu/Q \approx 0.02$ cm^{-1} (for a MDR with $Q \approx 10^6$ and optical frequency $\nu \approx 2 \times 10^4$ cm^{-1}). The fact that MDR-related peaks are observable in the spontaneous Raman scattering[19,20] and SRS[21] from droplets indicates that the spontaneous Raman cross section, and thus the Raman gain coefficient g_{Sc} of the droplet cavity, is enhanced relative to that of the bulk liquid in an optical cell. The QED enhancement[3] of the Raman gain is $\approx$100 for $x \approx 30$ and $Q \approx 10^4$.

Detailed QED calculations are necessary before the spatial dependence of the gain-enhancement factor is known.[22] Assuming that QED affects the spontaneous Raman transition rate and the fluorescence transition rate in the same way, the estimated ratio of the spatially averaged enhanced Raman gain coefficient g_{Sc} of a droplet cavity and the Raman gain coefficient g_S of a bulk liquid in an optical cell is as follows[3]:

$$g_{Sc}(\omega)/g_S(\omega) = \rho_c(\omega)/V\rho_{vac}(\omega), \tag{7}$$

where $\omega = 2\pi c\nu$ is the optical frequency, $\rho_{vac}(\omega) = \omega^2/\pi^2c^3$ is the density of states per unit volume in an infinite continuum, $V = 4\pi\mathbf{a}^3/3$ is the volume of the droplet, c is the speed of light in vacuum, and $\rho_c(\omega) = D/\Delta\omega_c = DQ/\omega$ is the density of discrete MDR's with linewidth $\Delta\omega_c$ and degeneracy D. For a spherical droplet, the azimuthal degeneracy is $D = 2n + 1$, where n is the mode number of the MDR. It is convenient to express ω in terms of the size parameter, which is defined as $x = 2\pi\mathbf{a}/\lambda = \omega\mathbf{a}/c$, where λ is the vacuum wavelength corresponding to the MDR with mode number n.

On substituting these expressions for $\rho_c(\omega)$, $\rho_{vac}(\omega)$, and V, one can express the enhanced Raman gain coefficient $g_{Sc}(x)$ in the droplet cavity relative to the gain coefficient in the bulk liquid in terms of MDR characteristics:

$$g_{Sc}(x)/g_S(x) = (3\pi/4)(2n + 1)Q/x^3. \tag{8}$$

The ratio of two enhanced Raman gain coefficients at two different MDR's at x and x' (with respective mode numbers n and n' and quality factors Q and Q') can be expressed as

$$g_{Sc}(x)/g'_{Sc}(x') = [(2n + 1)/(2n' + 1)](Q/Q')(x'/x)^3. \tag{9}$$

For MDR's with high Q's, the mode number n is bounded by $x < n < m(\omega)x$. From Eq. (8), the estimated enhancement of the Raman gain is $\approx$40 for droplets with $x = 472$ and MDR's with $Q \approx 10^6$ and $n \approx x$.

4. EXPERIMENTAL OBSERVATIONS WITH A MULTIMODE PUMP

Figure 3 shows the experimentally observed[7] time profiles of the multimode-input laser $I_{input}(t)$ and three orders of SRS [$I_{1S}(t)$, $I_{2S}(t)$, and $I_{3S}(t)$] in water droplets containing 5 M NH_4NO_3. The multiorder Stokes SRS is associated with the ν_1 vibrational mode of the nitrate ions. The following features in Fig. 3 are noteworthy: (1) the long delay time between $I_{input}(t)$ and $I_{1S}(t)$, (2) the much shorter delay time between $I_{1S}(t)$ and $I_{2S}(t)$ as well as between $I_{2S}(t)$ and $I_{3S}(t)$ (similar findings of the delay times have been reported when 70-ps laser pulses are used),[5] (3) the valleys of $I_{1S}(t)$ correspond to the peaks of $I_{2S}(t)$, (4) the valleys of the $I_{2S}(t)$ correspond to the peaks of $I_{3S}(t)$, and (5) the intensity valleys do not reach zero intensity.

The long time delay of the $I_{1S}(t)$ pulse with respect to the $I_{input}(t)$ pulse can be divided into two time intervals. The first interval is from the start of the input pulse $I_{input}(0)$ to an intensity level when $I_{input}(t)$ reaches the threshold intensity that causes the overall Raman gain to be greater than the total loss. During the second interval,

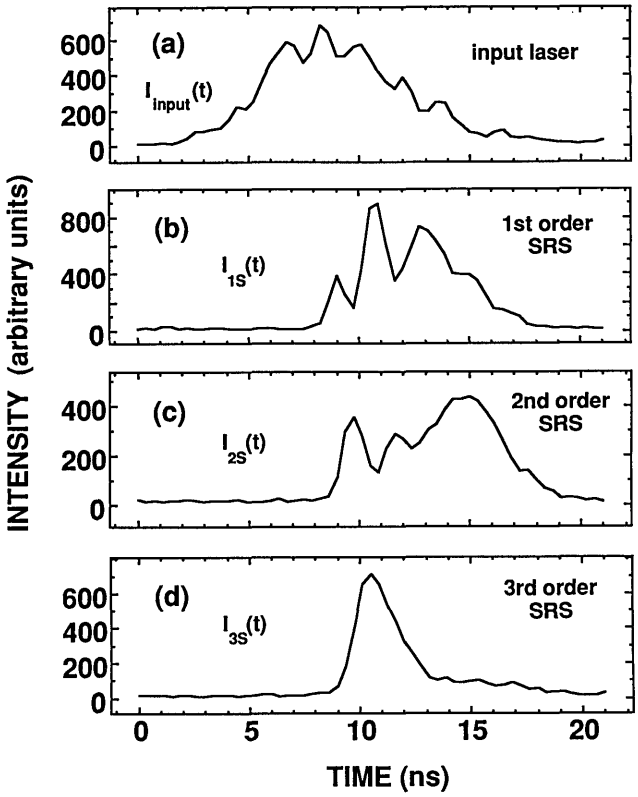

Fig. 3. Temporal profiles of the following experimentally observed pulses for aqueous NH_4NO_3 solution: (a) input laser $I_{input}(t)$, (b) first-order Stokes SRS $I_{1S}(t)$, (c) second-order Stokes SRS $I_{2S}(t)$, (d) third-order Stokes SRS $I_{3S}(t)$. The multiorder Stokes SRS is associated with the ν_1 symmetric vibrational mode of the nitrate ions; the time resolution is $\approx$0.4 ns. (After Ref. 7.)

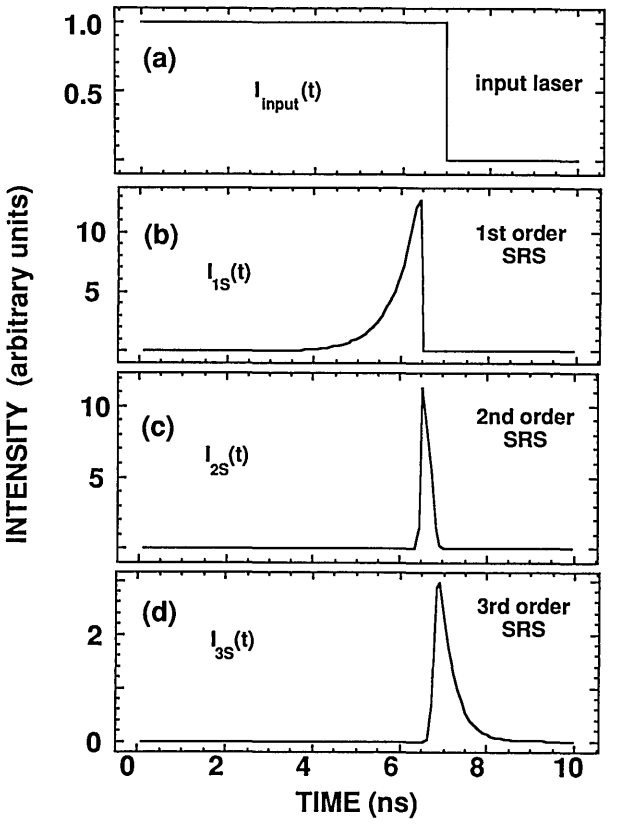

Fig. 4. (a) Idealized square-shaped laser time profile of 7-ns duration; using Eq. (5), calculated time profiles of (b) $I_{1S}(t)$, (c) $I_{2S}(t)$, and (d) $I_{3S}(t)$. The parameters used in the calculations are listed in Table 1. The Raman gain coefficient of the droplet cavity is $g_{Sc} = 0.31$ cm/GW. The wave-vector mismatch for all FWM processes is $\Delta k = 10^3\pi$ m^{-1}, which corresponds to a coherence time of $\tau_{coh} = 4$ ps. The time-averaged input-laser intensity is $\langle I_{input}\rangle_t = 0.8$ GW/cm^2.

$I_{1S}(t)$ builds up exponentially starting from the spontaneous Raman noise level I_{o1S} and begins to pump the second-order Stokes SRS. The short time delay observed between the $I_{2S}(t)$ and $I_{1S}(t)$ pulses indicates that the second-order Stokes SRS starts mainly from the parametric noise [generated by the FWM process associated with $I_{input}(t)$ and $I_{1S}(t)$] and, to a lesser extent, from the spontaneous Raman noise [generated by the spontaneous Raman scattering process with $I_{1S}(t)$]. Similarly, the short time delay between the $I_{3S}(t)$ and $I_{2S}(t)$ pulses indicates that the third-order Stokes SRS starts mainly from the parametric noise [generated by the FWM process associated with $I_{1S}(t)$ and $I_{2S}(t)$] and, to a lesser extent, from the spontaneous Raman noise [generated by the spontaneous Raman scattering process with $I_{2S}(t)$]. The correlations of the valleys of $I_{1S}(t)$ and the peaks of $I_{2S}(t)$ as well as the valleys of $I_{2S}(t)$ and the peaks of $I_{3S}(t)$ are indicative that the $(j + 2)$th-order Stokes SRS pulse is pumped by the $(j + 1)$th-order Stokes SRS pulse, which becomes depleted and requires the jth-order Stokes SRS pulse or the $I_{input}(t)$ pulse to repump the $(j + 1)$th-order Stokes SRS pulse. The experimental observation that the intensity valleys in Fig. 3 do not reach the zero-intensity level has never been explained. The present calculation indicates that the depth of the intensity valleys is related to the amount of phase matching among the waves involved in the FWM process.

5. CALCULATION OF SRS TEMPORAL PROFILES

A. Varying the Raman Gain

The growth and depletion of the various-order Stokes SRS is dependent on the Raman gain coefficient g_S [see Eq. (5)]. Therefore we need to investigate the dependence of the time profiles of the Stokes SRS on the Raman gain coefficient g_{Sc} of a droplet cavity, which is not the bulk-liquid value g_S but can be enhanced by QED effects.[3]

To isolate the effect of g_{Sc} on the time profiles of all the multiorder Stokes SRS intensities $I_{jS}(t)$, we initially assumed in our calculation a temporally square-shaped $I_{input}(t)$ with a duration $\tau_{input} = 7$ ns. After we isolate the effect of g_{Sc} on $I_{jS}(t)$, we then use the experimentally determined $I_{input}(t)$ in the computer simulations. The $I_{input}(\phi,t)$ is modeled by multiplying the temporal profile of the input-laser pulse $T_{input}(t)$ with the radially averaged internal-input intensity $\langle I_{input}(\phi)\rangle_r$ [see Fig. 2(a) and Eq. (4)]. Therefore the value of the enhanced Raman gain g_{Sc} will be dependent on the value of the radially integrated internal-input intensity. For the calculated results shown in Figs. 4–6, the wave-vector mismatches Δk_{jS} for all the FWM processes is selected to be equal, i.e., $\Delta k = \Delta k_{2S} = \Delta k_{3S} = \Delta k_{4S} = \Delta k_{bulk}$. The bulk-liquid value $\Delta k_{bulk} = 10^3\pi$ m^{-1} is calculated from the dispersion of the index of refraction of the liquid and corresponds to a coherence length $(l_{coh})_{bulk} = \pi/\Delta k_{bulk} = 10^3$ μm.

Figure 4 shows $I_{1S}(t)$, $I_{2S}(t)$, and $I_{3S}(t)$ for the square-shaped $I_{input}(t)$ with a time-averaged intensity of $\langle I_{input}\rangle_t = 0.8$ GW/cm^2. The Raman gain $g_{Sc} = 0.31$ cm/GW is selected so that the overall gain for the first-order Stokes SRS is slightly greater than the total loss. After $I_{input}(t)$ is on, the delay of $I_{1S}(t)$ is associated with the exponential

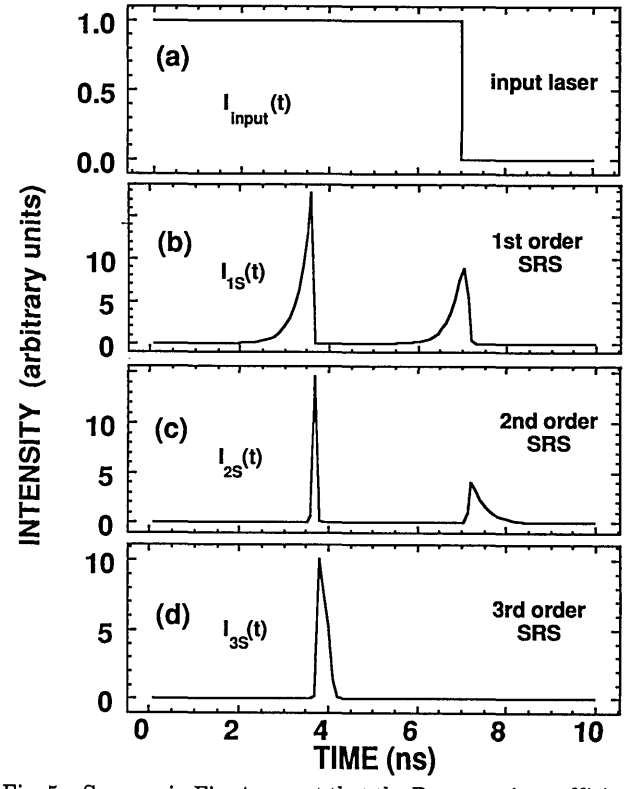

Fig. 5. Same as in Fig. 4, except that the Raman gain coefficient is increased to $g_{Sc} = 0.45$ cm/GW.

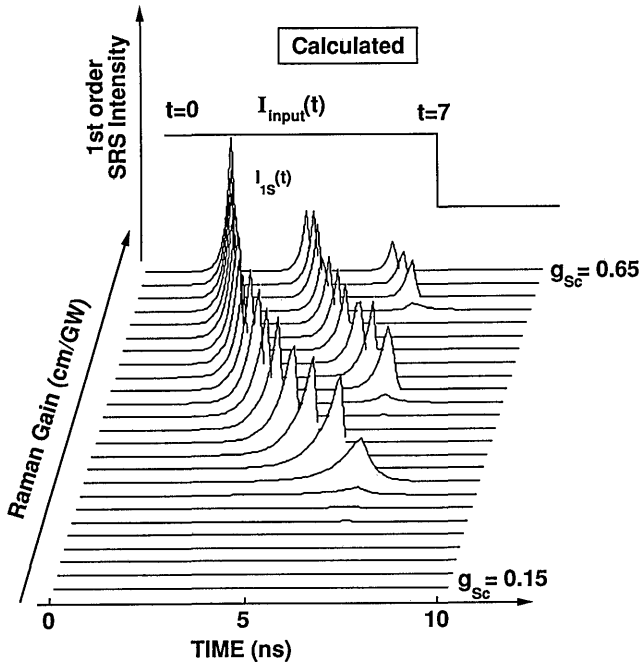

Fig. 6. Calculated time profiles of $I_{1S}(t)$ as a function of g_{Sc} with the square-shaped input-laser pulse with 7-ns duration and $\langle I_{input}\rangle_t = 0.8$ GW/cm^2 kept fixed. The Raman gain coefficient is varied from $g_{Sc} = 0.15$ cm/GW to $g_{Sc} = 0.65$ cm/GW in increments of $\Delta g_{Sc} = 0.02$ cm/GW. The wave-vector mismatch is fixed at $\Delta k = 10^3\pi$ m^{-1}, which corresponds to a coherence time of $\tau_{coh} = 4$ ps.

buildup of $I_{1S}(t)$, which starts from the spontaneous Raman noise at ν_{1S}. The exponentially rising portion of the $I_{1S}(t)$ is quite evident in the calculated pulse shape shown in Fig. 4(b). After $I_{1S}(t)$ becomes large, there is significant conversion to $I_{2S}(t)$, which starts mainly from the FWM-related parametric noise at ν_{2S}. After $I_{2S}(t)$ becomes large, $I_{3S}(t)$ soon appears. The fact that the delay time between $I_{1S}(t)$ and $I_{input}(t)$ is much longer than the delay time between $I_{2S}(t)$ and $I_{1S}(t)$ as well as between $I_{3S}(t)$ and $I_{2S}(t)$ is indicative that, while $I_{1S}(t)$ must start from spontaneous Raman noise, $I_{2S}(t)$ and $I_{3S}(t)$ can start from the more intense FWM-related parametric noise.

The calculated results shown in Figs. 4(b) and 4(c) indicate that the rise of $I_{2S}(t)$ is correlated to the decrease of $I_{1S}(t)$. Similarly, Figs. 4(c) and 4(d) show that the rise of $I_{3S}(t)$ is correlated to the decrease of $I_{2S}(t)$. At $\langle I_{input}\rangle_t = 0.8$ GW/cm^2, our calculation indicates that $I_{4S}(t)$ never achieves the SRS threshold and that, consequently, there is no intensity depletion for $I_{3S}(t)$. Therefore, after $I_{input}(t)$ is off, $I_{3S}(t)$ decreases with a decay time $\tau_{3S} = Q/2\pi c\nu_{3S}$, which is characteristic of the leakage of a wave in resonance with a MDR.

When $g_{Sc} = 0.31$ cm/GW is increased to $g_{Sc} = 0.45$ cm/GW while $\langle I_{input}\rangle_t = 0.8$ GW/cm^2 is kept fixed, comparison of the calculated results shown in Figs. 4 and 5 indicates that there is shortening of the delay time between $I_{1S}(t)$ and $I_{input}(t)$. Moreover, there is a slight decrease of the delay times between $I_{2S}(t)$ and $I_{1S}(t)$ and between $I_{3S}(t)$ and $I_{2S}(t)$. Furthermore, by use of an increased Raman gain, the exponential rise of $I_{1S}(t)$ is steeper and multiple pulses of $I_{1S}(t)$ and $I_{2S}(t)$ appear during the 7-ns $I_{input}(t)$. In Fig. 5 the growth and decay of $I_{1S}(t)$, $I_{2S}(t)$, and $I_{3S}(t)$ are again correlated because the growth of the $(j+1)$th-order Stokes SRS leads to the depletion of the jth-order Stokes SRS. In our model we did not include the depletion of $I_{4S}(t)$ (not shown in Figs. 4 and 5) because of pumping $I_{5S}(t)$. Therefore the decay of $I_{4S}(t)$ is caused only by the linear-absorption loss (α_{4S}) and the radiation leakage loss from the droplet cavity (L_{4S}). In our model we assumed that $L_{4S} > \alpha_{4S}$.

Because the appearance of the first pulses of $I_{1S}(t)$, $I_{2S}(t)$, and $I_{3S}(t)$ are well within the duration of $I_{input}(t)$ (see Fig. 5), the decay of these first pulses results mainly from the depletion associated with generating the next-higher-order Stokes SRS [except the generation of $I_{5S}(t)$]. The decay of the second pulse of $I_{1S}(t)$ [see Fig. 5(b)] is again due to the depletion effect. However, the decay of the second pulse of $I_{2S}(t)$ [see Fig. 5(c)] is not caused by intensity depletion because Fig. 5(d) shows that the second $I_{3S}(t)$ pulse did not have time to grow before $I_{input}(t)$ was off. Consequently the decay of the second pulse of $I_{2S}(t)$ is caused mainly by the cavity leakage L_{2S}, since in our model we also assumed that $L_{2S} > \alpha_{2S}$.

Figure 6 shows the temporal profile of $I_{1S}(t)$ as a function of increasing g_{Sc} (in increments of $\Delta g_{Sc} = 0.02$ cm/GW), starting from $g_{Sc} = 0.15$ cm/GW and ending at $g_{Sc} = 0.65$ cm/GW. $I_{input}(t)$ is still selected to have a square-shaped time profile with $\tau_{input} = 7$ ns and $\langle I_{input}\rangle_t = 0.8$ GW/cm^2. Throughout the computer simulation, $\Delta k_{jS} = \Delta k_{bulk} = 10^3\pi$ m^{-1} or $(l_{coh})_{jS} = (l_{coh})_{bulk} = 10^3$ μm. Note that the SRS threshold of $I_{1S}(t)$ is not reached for $g_S < 0.23$ cm/GW. As the Raman gain is increased from $g_{Sc} = 0.23$ cm/GW to $g_{Sc} = 0.31$ cm/GW, the exponentially rising portion of $I_{1S}(t)$ steepens, the peak value of $I_{1S}(t)$ increases, and the $I_{2S}(t)$ pulse (not shown) remains weak. As Raman gain is increased beyond $g_{Sc} = 0.31$ cm/GW, the falling portion of the first $I_{1S}(t)$ steepens, because more $I_{2S}(t)$ is generated, and the appearance of the second $I_{1S}(t)$ pulse is evident. Similar observations are noted on the rising and falling portion of the second $I_{1S}(t)$ pulse as the Raman gain is increased beyond $g_{Sc} = 0.31$ cm/GW. For $g_{Sc} > 0.61$ cm/GW, the third $I_{1S}(t)$ pulse appears. Not shown are the correlated growth of $I_{2S}(t)$ and $I_{3S}(t)$, both of which appear soon after the end of each $I_{1S}(t)$ pulse.

B. Varying the Phase Matching

Unlike the Raman gain, the phase matching (or the wave-vector mismatch) is not model dependent. The role of wave-vector mismatch Δk in the modified nonlinear-wave equations [Eqs. (5a) and (5b)] is investigated, while $g_{Sc} = 0.45$ cm/GW, $\langle I_{input}\rangle_t = 0.8$ GW/cm^2, and the square-shaped time profile with $\tau_{input} = 7$ ns are kept fixed. Throughout our simulation, we assumed, that $\Delta k = \Delta k_{2S} = \Delta k_{3S} = \Delta k_{4S}$. However, Δk is decreased from the estimated bulk-liquid value of $\Delta k_{bulk} = 10^3\pi$ m^{-1} [corresponding to $(l_{coh})_{bulk} = 10^3$ μm] to $\Delta k = 10\pi$ m^{-1} (corresponding to $l_{coh} = 10^5$ μm). The calculated time profiles of $I_{1S}(t)$, $I_{2S}(t)$, and $I_{3S}(t)$ are shown in Fig. 7. Comparison of Figs. 5 and 7 shows the following effects of decreasing Δk: (1) the $I_{1S}(t)$ pulse has a shorter delay time, a decreased intensity, and a lengthened pulse duration; (2) the $I_{2S}(t)$ pulse has a shorter delay time; (3) the intensity valley of the $I_{jS}(t)$ does not reach zero; and (4) the delay time for the second and subsequent pulses of $I_{1S}(t)$, $I_{2S}(t)$, and $I_{3S}(t)$ shortens.

The temporal profiles of $I_{1S}(t)$, $I_{2S}(t)$, and $I_{3S}(t)$ calcu-

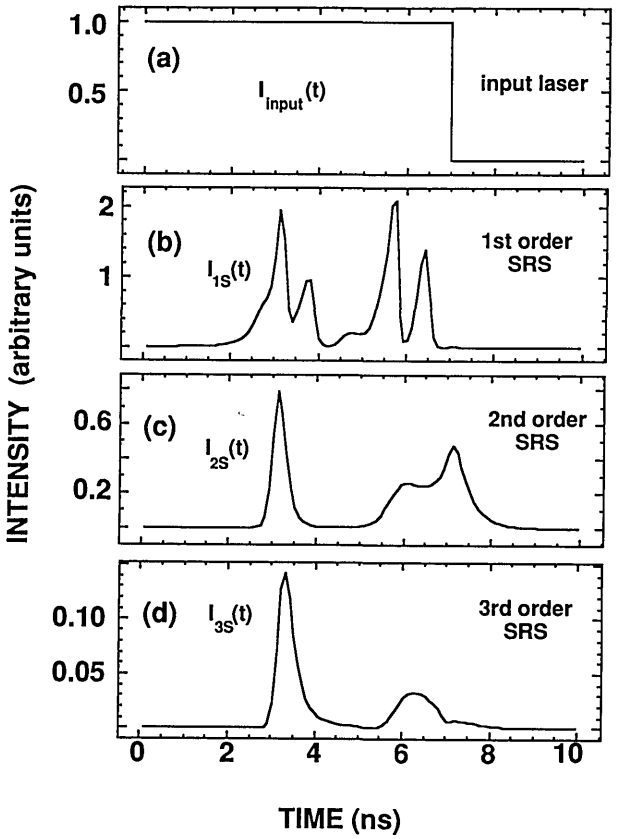

Fig. 7. Same as in Fig. 5, except that the wave-vector mismatch is decreased to $\Delta k \approx 10\pi\ \mathrm{m}^{-1}$, which corresponds to a coherence time of $\tau_{coh} = 0.4$ ns.

lated assuming that $\Delta k = 10\pi\ \mathrm{m}^{-1}$ (shown in Fig. 7) resemble the experimentally observed pulse shapes (shown in Fig. 3) better than those calculated assuming that $\Delta k = \Delta k_{bulk} = 10^3\pi\ \mathrm{m}^{-1}$ (shown in Fig. 5). Consequently because Δk affects the time profiles of multiple SRS pulses, we conclude that the FWM processes are important in coupling the various-order Stokes SRS in droplets. Furthermore, because decreasing Δk improves the agreement between the calculated and the experimentally observed time profiles of multiple SRS pulses, we conclude that the phase matching of nonlinear waves in resonance with MDR's is better than the phase matching of nonlinear plane waves in an optical cell, i.e., $\Delta k < \Delta k_{bulk}$.

The concept of phase matching in a droplet is meaningful only if the nonlinear waves generated at one region can be partially retained in the droplet (or not leak from the droplet) and, thereby, be summed coherently at another region of the droplet. Because the radiation leakage from the droplet is often expressed in terms of a cavity lifetime ($\tau_c = Q/\omega$), it is convenient to express phase matching by a coherence time τ_{coh}, which can be defined as

$$\tau_{coh} = l_{coh}\frac{m(\omega)}{c} = \left(\frac{\pi}{\Delta k}\right)\frac{m(\omega)}{c}. \tag{10}$$

As Δk is decreased from the bulk value $\Delta k_{bulk} = 10^3\pi\ \mathrm{m}^{-1}$, the coherence time τ_{coh} lengthens. At $\Delta k \approx 10\ \mathrm{m}^{-1}$, $\tau_{coh} \approx 1$ ns, which is comparable with the measured cavity lifetime $\tau_c \approx 1$ ns. As long as $\tau_{coh} < \tau_c$, the nonlinear waves grow as $(l_{coh})^2$ without experiencing much leakage loss. However, when $\tau_{coh} \geq \tau_c$, the nonlinear waves no longer grow proportionally to $(l_{coh})^2$ because the droplet cavity can no longer retain the nonlinear wave generated one l_{coh} away. When τ_{coh} becomes comparable with or greater than the input-laser pulse duration $\tau_{input} \approx 7$ ns (corresponding to $\Delta k \approx 1\ \mathrm{m}^{-1}$), further increase of τ_{coh} (or decrease of Δk) does not have any appreciable effect on the time profiles of $I_{1S}(t)$, $I_{2S}(t)$, and $I_{3S}(t)$. Once $\tau_{coh} = \tau_{input}$, a further increase of τ_{coh} should not affect nonlinear coupling because during $I_{input}(t)$ the nonlinear waves are always phase matched.

Figure 8 shows the evolution of $I_{1S}(t)$ as Δk is decreased from $\Delta k_{bulk} = 10^3\pi\ \mathrm{m}^{-1}$ to $\Delta k = 0.1\pi\ \mathrm{m}^{-1}$ for a fixed square-shaped input pulse with $\langle I_{input}\rangle_t = 0.8\ \mathrm{GW/cm^2}$, $\tau_{input} = 7$ ns, and Raman gain $g_{Sc} = 0.45$ cm/GW. The dominant effects of increasing τ_{coh} (or decreasing Δk) are to raise the valley intensity of $I_{1S}(t)$ and to depress the peak intensity of $I_{1S}(t)$ (see Fig. 8) and also $I_{2S}(t)$ and $I_{3S}(t)$ (not shown). Note that the selected Raman gain coefficient for the droplet is 3× larger than that for the cell (see Table 1). This enhanced Raman gain coefficient value is dependent on the assumption that the MDR has a flat radial intensity distribution in the $\mathbf{a}/m(\nu) < r < \mathbf{a}$ region. In our model we averaged the internal-pump intensity along the r direction in the $\mathbf{a}/m(\nu) < r < \mathbf{a}$ region and used the radially averaged value of the internal input-laser intensity $\langle I_{input}(\phi)\rangle_r$ [see Eq. (1)] as the pump for the multiorder Stokes SRS. Once the l value of the MDR is known, it is possible to calculate the spatial overlap between the internal input-laser intensity and the radial distribution

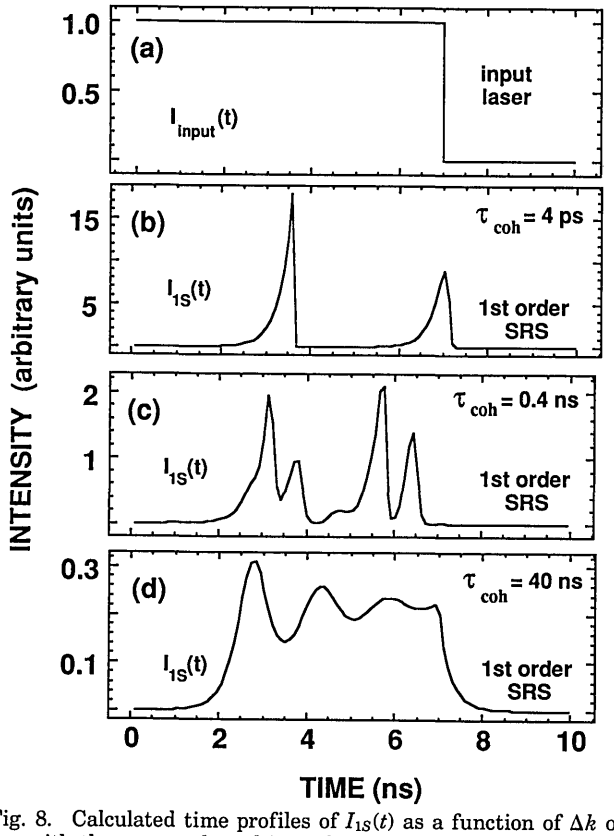

Fig. 8. Calculated time profiles of $I_{1S}(t)$ as a function of Δk or τ_{coh} with the square-shaped input-laser pulse with 7-ns duration and $\langle I_{input}\rangle_t = 0.8\ \mathrm{GW/cm^2}$ kept fixed. The wave-vector mismatch is varied from $\Delta k = 10^3\pi\ \mathrm{m}^{-1}$ to $\Delta k = 0.1\pi\ \mathrm{m}^{-1}$. The corresponding variation of τ_{coh} is from $\tau_{coh} = 4$ ps to $\tau_{coh} = 40$ ns. The Raman gain coefficient is fixed at $g_{Sc} = 0.45$ cm/GW.

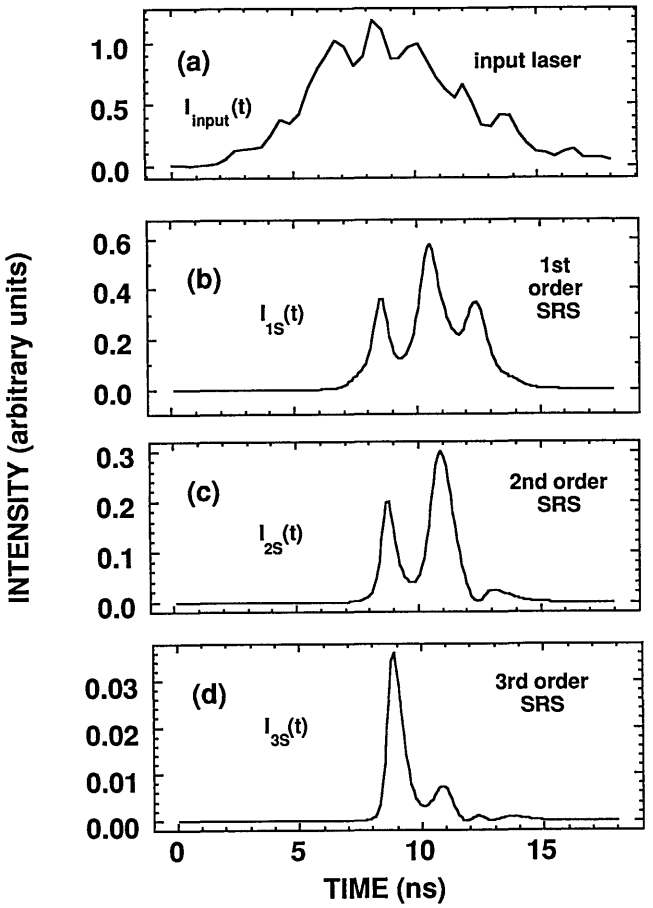

Fig. 9. (a) Experimentally observed laser pulse $I_{input}(t)$ (normalized) (after Ref. 7); using Eq. (5), calculated time profiles of (b) $I_{1S}(t)$, (c) $I_{2S}(t)$, and (d) $I_{3S}(t)$. To achieve reasonable agreement with the experimental time profiles (shown in Fig. 3), the Raman gain coefficient is adjusted to be $g_{Sc} = 0.45$ cm/GW and the wave-vector mismatch is adjusted to be $\Delta k = 2.18\ \mathrm{m}^{-1}$ (corresponding to $\tau_{coh} = 6.4$ ns). All other parameters used in the calculations of Eq. (5) for nitrate ions in water droplets are listed in Table 1.

of the particular MDR. Such an overlap integral of the internal input-laser intensity and the MDR would result in a different enhancement factor for each MDR within the Raman gain profile.

C. Simulation of the Experimental Results

Having investigated the separate roles of g_S and Δk with a square-shaped input-laser pulse $I_{input}(t)$, the experimentally observed time profile $I_{input}(t)$, shown in Fig. 3(a), is now used in our numerical simulation. Figure 9(a) shows $I_{input}(t)$ used to calculate $I_{1S}(t)$, $I_{2S}(t)$, and $I_{3S}(t)$ [shown in Figs. 9(b), 9(c), and 9(d), respectively]. When we select $g_{Sc} = 0.45$ cm/GW and $\Delta k = 2.18\ \mathrm{m}^{-1}$ (corresponding to $\tau_{coh} = 6.39$ ns), the calculated $I_{1S}(t)$, $I_{2S}(t)$, and $I_{3S}(t)$ pulses (see Fig. 9) compare reasonably well with the observed time profiles of $I_{1S}(t)$, $I_{2S}(t)$, and $I_{3S}(t)$ (see Fig. 3). For the calculated results shown in Fig. 9, all the other parameters needed in Eq. (5) are tabulated in Table 1.

6. WAVE EQUATIONS FOR SBS AND SRS WITH A SINGLE-MODE PUMP

When a single-mode laser is used to irradiate micrometer-size droplets, the SBS threshold is 3× lower than the SRS threshold. When viewed along the y axis, the SBS appears as two green dots located in the equatorial plane at $x = \pm\mathbf{a}$. Thus, in our simulation, the detected SBS waves are assumed to be associated with the nonlinear waves that are confined to the equatorial plane and circulating in the $\pm\phi$ directions. In order to describe the growth and decay of the SBS intensity $I_B(t)$ as well as $I_{jS}(t)$ in a droplet, we modified the coupled one-dimensional nonlinear-wave equations for the generation of SBS and multiorder Stokes SRS in an optical cell.[8,14] As we did previously for the multimode input-laser pump case, we transformed the incremental length dz of an optical cell to the incremental arc length $\mathbf{a}d\phi$ at the droplet rim. The distance z from the front of the optical cell ($z = 0$) is transformed to $\mathbf{a}\phi$ starting from $\phi = 0°$, where $I_{input}(r, \phi)$ has a maximum. The total number of round trips around the droplet rim is equal to $\phi/360°$.

A. Nonlinear-Optical Wave Equations

We attempt to simulate the observed time profiles of $I_B(t)$ and $I_{1S}(t)$ by modifying the coupled one-dimensional wave equations for the generations of SBS and SRS in an optical cell. The following wave equations[8,14] are used to describe the growth and decay of the SBS and SRS waves circulating in the $\pm\phi$ directions at the droplet rim and in the equatorial plane:

$$\frac{dE_B}{\mathbf{a}d\phi} = \left[\frac{g_B}{2}I_{input} - \frac{g_S}{2}\frac{\nu_B}{\nu_{1S}}I_{1S} - \frac{\alpha_B}{2} - \frac{L_B}{2}\right]E_B - \frac{g_S}{2}\frac{\nu_B}{\nu_{1S}}E_{2S}{}^{*}E_{1S}E_{1S}\exp(i\Delta k_{2SB}\mathbf{a}\phi) - \sum_{j=3}^{j_{final}}\frac{g_S}{2}\frac{\nu_B}{\nu_{1S}}E_{jS}{}^{*}E_{1S}E_{(j-1)S}\exp(i\Delta k_{jSB}\mathbf{a}\phi), \quad (11a)$$

$$\frac{dE_{1S}}{\mathbf{a}d\phi} = \left[\frac{g_S}{2}(I_B + I_{input} - I_{2S}) - \frac{\alpha_{1S}}{2} - \frac{L_{1S}}{2}\right]E_{1S} - \frac{g_S}{2}E_{input}E_{1S}{}^{*}E_{2S}\exp(i\Delta k_{2S}\mathbf{a}\phi) - \frac{g_S}{2}E_BE_{1S}{}^{*}E_{2S}\exp(i\Delta k_{2SB}\mathbf{a}\phi) - \sum_{j=3}^{j_{final}}\frac{g_S}{2}E_{input}E_{(j-1)S}{}^{*}E_{jS}\exp(i\Delta k_{jS}\mathbf{a}\phi) - \sum_{j=3}^{j_{final}}\frac{g_S}{2}E_BE_{(j-1)S}{}^{*}E_{jS}\exp(i\Delta k_{jSB}\mathbf{a}\phi). \quad (11b)$$

In addition to the notations used in Eqs. (5a) and (5b), the following new notations are used: g_B is the Brillouin gain coefficient; $\nu_B = \nu_{input} - \nu_{ac}$ is the Brillouin frequency, where ν_{ac} is the acoustic-wave frequency; α_B is the linear absorption loss at the Brillouin frequency ν_B; L_B is the droplet-cavity loss because of the leakage of SBS from the droplet; E_B is the SBS electric field; I_B is the SBS intensity; $\Delta k_{2SB} = (k_{2S} + k_{SBS} - 2k_{1S})$ is the wave-vector mismatch among the internal wave vectors of the second-order Stokes SRS (k_{2S}), the SBS (k_{SBS}), and the two first-order Stokes SRS ($2k_{1S}$); and $\Delta k_{jSB} = [k_{jS} + k_{SBS} - k_{1S} - k_{(j-1)S}]$ is the wave-vector mismatch among the wave vectors of the jth-order Stokes SRS (k_{jS}), the SBS (k_{SBS}), the first-order Stokes SRS (k_{1S}), and the $(j-1)$th-order Stokes SRS [$k_{(j-1)S}$].

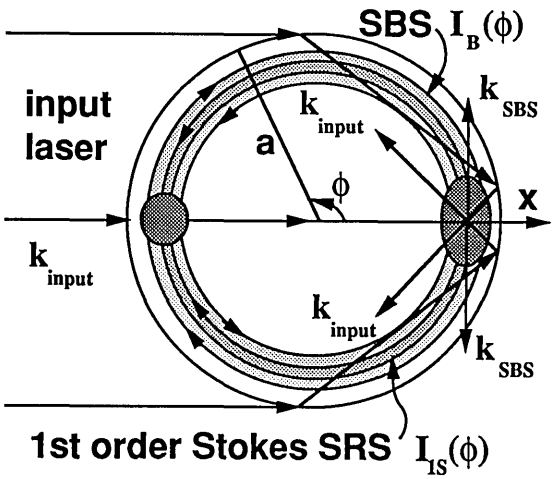

Fig. 10. Schematic of the spatial distribution of the intensity (shaded areas) and the rays of the input-laser, SBS, and first-order Stokes SRS waves in the droplet equatorial plane. The intensity maximum of the input-laser beam is concentrated on the shadow side of the droplet. There is a spread of the input-laser wave vector k_{input}. The generated SBS and SRS waves are on MDR's, which are represented as two counterpropagating traveling waves around the droplet rim. The wave vectors of the SBS (k_{SBS}) and SRS (k_{1S}) are always tangential to the droplet rim since both waves are on MDR's. The Brillouin gain coefficient and the Brillouin frequency are functions of the angle between k_{SBS} and k_{input}.

In the droplet, I_B starts from the spontaneous Brillouin noise I_{oB} (at ν_B), which is generated predominantly in the region of enhanced laser intensity $I_{input}(\phi = 0)$ inside the droplet. Based on spontaneous Brillouin and Raman scattering experiments in an optical cell,[23] $g_B > g_S$. In droplets, g_B is also deduced to be greater than g_S because the threshold for SBS is lower than that for SRS and the delay time of the $I_B(t)$ pulse is shorter than that of the $I_{1S}(t)$ pulse.[4]

The depletion of E_B because of pumping SRS is described by the $(-g_S\nu_B I_{1S}E_B/2\nu_{1S})$ term in Eq. (11a). The coupled wave equation for E_{1S} [see Eq. (11b)] now incorporates the gain from the SBS pump ($g_S I_B E_{1S}/2$ term) and the single-mode input-laser pump ($g_S I_{input}E_{1S}/2$ term). Similar to the wave equation for the multimode $I_{input}(t)$ pumping $I_{1S}(t)$, the depletion of E_{1S} is caused by pumping $I_{2S}(t)$ [$-g_S I_{2S}E_{1S}/2$ term in the Eq. (11b)]. The $I_{1S}(t)$ starts from the spontaneous Raman noise I_{o1S} (at ν_{1S}) that is generated in the following two regions: (1) the two localized regions of enhanced laser intensity $I_{input}(\phi, t)$ inside the droplet (see Fig. 2) and (2) a uniform region around the droplet rim where the SBS waves are confined.

The wave equation for E_{2S}, with single-mode input-laser pumping, remains the same as Eq. (5b) with multimode input-laser pumping. The FWM process involving E_{2S} is incorporated into the second term on the right-hand side of Eq. (11a). The third terms in Eqs. (11a) and (11b) are FWM terms associated with the jth-order Stokes SRS, where $j \geq 3$. For the generation of the jth-order Stokes SRS, there are always two initial sources of E_{jS}, one from the spontaneous Raman noise and another from the FWM-related parametric noise. In our simulation, with single-mode input radiation, we neglected the growth of E_{3S} and higher-order Stokes SRS waves.

Figure 10 illustrates the rays of the input-laser beam and the waves of the SBS and the SRS inside the droplet. The intensity of the input-laser beam is concentrated mainly on the shadow side of the droplet. The generated SBS and SRS waves are on two different MDR's, which are both localized around the droplet rim but have different radial distributions. The SBS wave vector k_{SBS} is always tangent to the droplet rim. The angle ϕ_B between the input-laser wave vector k_{input} and k_{SBS} affects ν_B and g_B. The same numerical methods used in calculating the time profiles of $I_{jS}(t)$ with a multimode $I_{input}(t)$ can be repeated for the case of the single-mode $I_{input}(t)$ pumping $I_B(t)$, and $I_{input}(t)$ together with $I_B(t)$ pumping $I_{1S}(t)$.

B. Brillouin Frequency Shift and Gain

In contrast to the Raman frequency ν_{1S}, which is a property of the medium and constant throughout the droplet, the Brillouin frequency ν_B is a function of the acoustic phonon wave vector k_{ac} and frequency ν_{ac}, which are not constant throughout the droplet. The Brillouin frequency $\nu_B = \nu_{input} - \nu_{ac}$ is dependent on the angle between k_{input} and the wave vector of the Brillouin wave k_B. The maximum ν_B occurs for backward scattering ($\phi_B = \pi$) and is related to the input-laser frequency ν_{input} as follows[8,23]:

$$\nu_B(\phi_B = \pi) = \nu_{input} - \nu_{ac}(\phi_B = \pi), \tag{12a}$$

where

$$\nu_{ac}(\phi_B = \pi) = k_{ac}(\phi_B = \pi)/2\pi = k_{input}/\pi = 2\nu_{input}m(\nu_{input}). \tag{12b}$$

The acoustic wave vector for backward scattering is $k_{ac}(\phi_B = \pi)$. For most liquids $\nu_{ac}(\phi_B = \pi) = 0.2$ cm^{-1}.

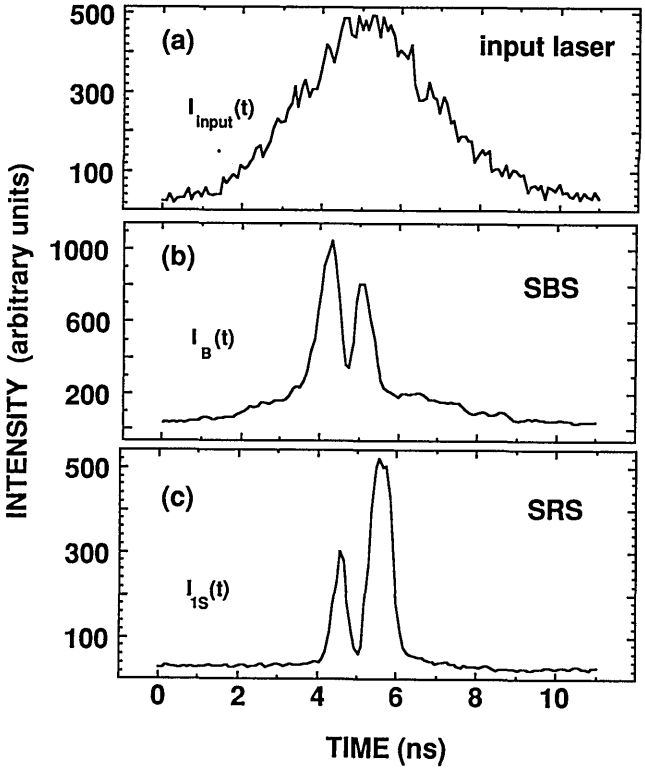

Fig. 11. Temporal profiles of the experimentally observed pulses of (a) $I_{input}(t)$, (b) $I_B(t)$, and (c) $I_{1S}(t)$ for ethanol droplets, with a time resolution of ≈0.1 ns. (After Ref. 4.)

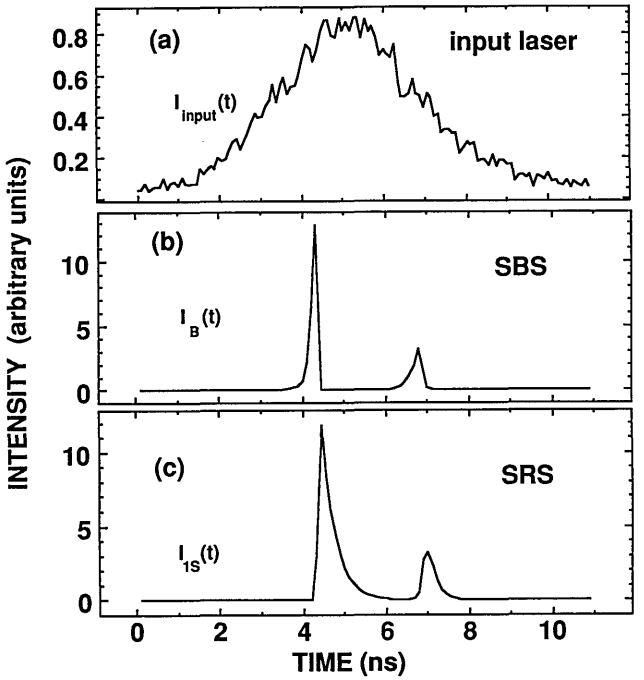

Fig. 12. (a) Experimentally observed time profile (after Ref. 4) of the input-laser pulse $I_{input}(t)$ (normalized); calculated time profiles of (b) $I_B(t)$ and (c) $I_{1S}(t)$. All the other parameters used in the calculations of Eq. (11) for ethanol droplets are listed in Table 2. To achieve reasonable agreement with the experimental time profiles (shown in Fig. 11), the Raman gain coefficient is adjusted to be $g_{Sc} = 2.0$ cm/GW, and the Brillouin gain coefficient is adjusted to be $g_{Bc} = 3.0$ cm/GW. The wave-vector mismatch is $\Delta k = 10^3 \pi\ \mathrm{m}^{-1}$ (corresponding to $\tau_{coh} = 4$ ps).

As a function of the angle ϕ_B, the Brillouin shifts are $\nu_{ac}(\phi_B) = \nu_{ac}(\phi_B = \pi)\sin(\phi_B/2)$. However, because of refraction of the input-light rays caused by the droplet morphology, there is a spread of angles for k_{input}. Consequently ϕ_B is distributed around $\phi_B = 90°$ and extends from $\phi_B = 43°$ to $\phi_B = 137°$ (i.e., a spread $\Delta\phi_B = 94°$). This spread of $\Delta\phi_B$ gives rise to a range of Brillouin shifts $\Delta\nu_{ac}(\Delta\phi_B) \approx 0.1\ \mathrm{cm}^{-1}$. Therefore the inhomogeneously broadened[23] Brillouin linewidth is $\Delta\nu_{ac}(\Delta\phi_B) \approx 0.1\ \mathrm{cm}^{-1}$, whereas the homogeneously broadened Brillouin linewidth is typically $0.02\ \mathrm{cm}^{-1}$.

In contrast to the Raman gain coefficient g_S, which is constant (although enhanced to g_{Sc}) near the droplet rim, the Brillouin gain coefficient g_B is a function of k_{ac} and ν_{ac} and therefore is not constant near the droplet rim. The experimental value[8] determined in an optical cell is $g_B(\phi_B = \pi) = 13.0$ cm/GW with $\lambda_{input} = 632.8$ nm.

The QED effect, which can enhance the Raman gain g_S of liquids in the form of micrometer-size droplets, can also enhance the Brillouin gain g_B. However, there may be differences between the QED treatment of the Raman and Brillouin processes. For the Raman case, the homogeneously broadened vibrational linewidth (i.e., with optical phonon lifetime limited) is typically $\Delta\nu_{vib} \approx 10\ \mathrm{cm}^{-1}$. Thus $\Delta\nu_{vib} \gg \Delta\nu_c$, where $\Delta\nu_c$ is the droplet cavity or MDR linewidth, which is $\Delta\nu_c = \nu/Q \approx 0.02\ \mathrm{cm}^{-1}$, for a MDR with frequency $\nu \approx 2 \times 10^4\ \mathrm{cm}^{-1}$ and $Q \approx 10^6$. However, for the Brillouin case the acoustic-phonon lifetime-broadened homogeneous-Brillouin linewidth $\Delta\nu_{ac} \approx 0.02\ \mathrm{cm}^{-1}$ is comparable with $\Delta\nu_c = \nu/Q \approx 0.02\ \mathrm{cm}^{-1}$. Thus the Brillouin process is in the critical coupling QED regime,[3] while the Raman process is in the strong-coupling QED regime. Consequently the QED enhancement factor for g_B may not be the same as for g_S. Because we are not able to estimate the QED enhancement factor, we should treat the Brillouin gain g_{Bc} in the droplet cavity as an adjustable parameter in our model.

For the Raman case it is always possible to find MDR's within the spontaneous Raman linewidth ($10\ \mathrm{cm}^{-1}$) because the density of MDR's[11] is typically two MDR's within a 1-cm^{-1} interval. So the QED can enhance the maximum of the Raman gain profile $g_S(\nu)$. For the Brillouin case, even the inhomogeneously broadened Brillouin linewidth $\Delta\nu_{ac}(\Delta\phi_B) \approx 0.1\ \mathrm{cm}^{-1}$ is less than the average spacing of MDR's. Thus it is not always possible to find MDR's within the Brillouin linewidth. The QED can enhance the Brillouin gain $g_B(\nu)$ only if there is some frequency overlap between the inhomogeneously broadened Brillouin gain profile and a MDR, which may not necessarily be at the frequency corresponding to the maximum of $g_B(\nu)$. Depending on the frequency overlap of the MDR and the Brillouin gain profile, only a fraction of the k_{input} is effective in pumping the SBS. Consequently the effective $I_{input}(\phi)$ for pumping the SBS in the single-mode laser experiment can be lower than that for pumping the SRS in the multimode-laser experiment.

During the round trip in the $\pm\phi$ directions around the droplet rim, the SRS wave experiences a ϕ-dependent Raman gain because of the ϕ dependence of $I_{input}(\phi)$ and a ϕ-independent gain because $I_B(\phi)$ is on a MDR. However, the SBS wave experiences a ϕ-dependent gain not only because of $I_{input}(\phi)$ but also because the Brillouin gain coefficient g_B is dependent on ϕ_B. In our numerical simulation of the nonlinear waves in a droplet, we assumed a constant angularly averaged g_{Bc} because we are unable to account for the ϕ dependence of g_{Bc}. Consequently we assumed that the overall Brillouin gain and Raman gain depend only on $I_{input}(\phi)$.

7. EXPERIMENTAL OBSERVATIONS WITH A SINGLE-MODE PUMP

When the second-harmonic output of a single-mode Q-switched Nd:YAG laser is used to irradiate ethanol droplets, the observed SBS spectra are analyzed with a Fabry–Perot interferometer.[4] The temporal profiles of the laser, SBS, and SRS pulses from ethanol droplets are simultaneously detected with a streak camera. The first SBS pulse always occurred earlier than the first SRS pulse, i.e., the time delay between $I_B(t)$ and $I_{input}(t)$ is shorter than that between $I_{1S}(t)$ and $I_{input}(t)$. Furthermore the subsequent pulses of SBS and SRS are temporally correlated; i.e., the minimum of the $(n + 1)$th SBS pulse occurs when the nth SRS pulse reaches a maximum. The experimentally observed[4] time profiles of $I_{input}(t)$, $I_B(t)$, and $I_{1S}(t)$, all with a single-mode input laser, are shown in Figs. 11(a), 11(b), and 11(c), respectively.

8. CALCULATION OF SBS AND SRS TEMPORAL PROFILES

Figure 12(a) shows the experimentally observed temporal profile of $I_{input}(t)$, and Figs. 12(b) and 12(c) show the calculated SBS and SRS pulses, respectively. All the parame-

Table 2. Parameters for the Single-Mode Laser Pumping SBS and SRS

Parameter	Value	Reference
Brillouin gain coefficient of ethanol	$g_B(\phi_{SBS} = \pi) = 13.0$ cm/GW	8
Raman gain coefficient of ethanol	$g_S = 5.11$ cm/GW	14
Absorption loss (at ν_B)	$\alpha_B = 0.1$ m^{-1}	24
Absorption loss (at ν_{1S})	$\alpha_{1S} = 0.133$ m^{-1}	24
Absorption loss (at ν_{2S})	$\alpha_{2S} = 0.2$ m^{-1}	24
Q factor of MDR's	$Q = 10^6$	18
Leakage loss (at ν_B)	$L_B = 2\pi\nu_B m(\nu_B)/Q$ m^{-1}	18
Leakage loss (at various Stokes ν_{jS})	$L_{jS} = 2\pi\nu_{jS} m(\nu_{jS})/Q$ m^{-1}	18
Brillouin shift for ethanol	$\nu_{ac} = 0.142$ cm^{-1}	4
Raman shift for ethanol	$\nu_{vib} = 2928$ cm^{-1}	4
Input-laser frequency	$\nu_{input} = 18\,797$ cm^{-1}	4
Time-averaged input-laser intensity	$\langle I_{input}\rangle_t = 0.3$ GW/cm^2	4
Droplet radius	$\mathbf{a} = 45$ μm	4
Refractive index of ethanol	$m(\nu) = 1.36$	25
Wave-vector mismatch for ethanol	$\Delta k = 10^3\pi$ m^{-1}	26

ters needed to solve Eq. (11) are listed in Table 2. Reasonable agreement between the experimentally observed and calculated time profiles of $I_B(t)$ and $I_{1S}(t)$ is obtained if we adjust $g_{Bc}(\phi_B = \pi) = 3.0$ cm/GW and $g_{Sc} = 2.0$ cm/GW. The Brillouin gain coefficient is lower than the cell values calculated for the range of ϕ_B's in the droplet. However, our model assumes that all the incident input-laser rays can pump SBS and does not include the k_{input} dependence of g_{Bc}. In reality only a fraction of the $\langle I_{input}\rangle_t = 0.3$ GW/cm^2 can be used to pump SBS. A lower effective value of $\langle I_{input}\rangle_t$ will correspondingly increase the value of g_{Bc}.

In Eq. (11) the SRS wave is assumed to be pumped by the SBS wave as well as by the input laser. On the basis of our numerical simulations, we deduced that strong correlation between the SBS and SRS pulses exists only if the SBS wave mainly pumps the SRS wave. That is, the SRS wave is only weakly pumped by the input laser. In fact, a similar deduction can be made from the experimental results.[4] Note from Fig. 11(c) the first SRS pulse reaches a maximum after the first SBS pulse is depleted, and the more intense second SRS pulse occurs after the second SBS pulse is depleted.

9. CONCLUSIONS

We modified the standard one-dimensional coupled nonlinear-wave equations in an optical cell to accommodate the droplet geometry and the droplet-cavity characteristics. We used a heuristic model to simulate the generation and coupling of nonlinear waves in droplets. In particular, we calculated the time profiles of various orders of Stokes SRS pulses and of SBS pulses from droplets. The agreement between the calculated and the experimentally observed delay times as well as the correlated growth and decay of nonlinear pulses is reasonable if the gain coefficients and the wave-vector mismatch are two adjustable parameters.

For multimode-laser input, the growth and decay of the first- through fourth-order Stokes SRS are calculated as a function of the Raman gain coefficient and wave-vector mismatch for FWM. Raman gain coefficient is adjusted until the calculated and the experimentally observed delay time between the first-order Stokes SRS pulse and the input-laser pulse agree. The adjusted Raman gain coefficient is noted to be 3× larger than the Raman gain coefficient for nitrate ions in an optical cell of water. It is uncertain at this time whether the enhancement of the Raman gain coefficient in droplets is consistent with that predicted from QED enhancement effects. The enhanced Raman gain coefficient value is dependent on the assumption that the MDR, which provides the necessary feedback for the nonlinear waves, has a flat radial distribution in the $\mathbf{a}/m(\nu) < r < \mathbf{a}$ region of the droplet. A model using the actual radial-intensity distribution of the MDR would have resulted in a different enhancement factor. The wave-vector mismatch (or the coherence time) for the FWM process is adjusted until reasonable agreement is achieved between the calculated and the experimentally observed temporal correlation among the various-order Stokes SRS. The adjusted coherence time is noted to be 10^3× longer than for water in an optical cell. The improvement of Δk (or the coherence time) is an indication that phase matching among droplet MDR's is improved relative to phase matching among plane waves in an optical cell of water.

For single-mode laser input, the growth and decay of the SBS and SRS are calculated as a function of the angle-averaged Brillouin gain coefficient. The Brillouin gain coefficient is adjusted until the calculated and the experimentally observed delay times between the SBS pulse and the input-laser pulse agree. The optimum angle-averaged Brillouin gain coefficient is 0.2× the maximum Brillouin gain coefficient $g_B(\phi_B = \pi)$ measured in the backscattering direction in an optical cell of ethanol. This decrease of the Brillouin gain coefficient for a droplet may be caused by the angular spread of the ϕ_B and the possibility that the MDR is not at the maximum of the inhomogeneously broadened Brillouin gain profile. The numerical simulation is consistent with the experimental observation that the SBS wave is more effective than the input-laser beam (unfocused and not on an input resonance) in pumping the SRS wave.

ACKNOWLEDGMENTS

We gratefully acknowledge the partial support of this research by the U.S. Air Force Office of Scientific Research (grant 91-0150) and the U.S. Department of Energy, Energy Conversion and Utilization Technologies Program

(contract DE AS04-87-AL42879). We thank D. Q. Chowdhury of Clarkson University and Yale University for many helpful discussions.

REFERENCES AND NOTES

1. C. F. Bohren and D. R. Huffman, *Absorption and Scattering of Light by Small Particles* (Wiley, New York, 1983), pp. 93–104.
2. E. M. Purcell, "Spontaneous emission probabilities at radio frequencies," Phys. Rev. **69,** 681–681 (1946).
3. S. C. Ching, H. M. Lai, and K. Young, "Dielectric microspheres as optical cavities: thermal spectrum and density of states," J. Opt. Soc. Am. B **4,** 1995–2003 (1987); "Dielectric microspheres as optical cavities: Einstein *A* and *B* coefficients and level shift," J. Opt. Soc. Am. B **4,** 2004–2009 (1987).
4. J.-Z. Zhang, G. Chen, and R. K. Chang, "Pumping of stimulated Raman scattering by stimulated Brillouin scattering within a single droplet: input laser linewidth effects," J. Opt. Soc. Am. B **7,** 108–115 (1990).
5. S.-X. Qian, S. Yuan, Y. Li, H. Wang, X. Huang, and Z. Yu, "Comparison between the temporal characteristics of picosecond SRS from the cell and SRO from the droplet," Opt. Commun. **74,** 414–418 (1990).
6. R. G. Pinnick, A. Biswas, P. Chylek, R. L. Armstrong, H. Latifi, E. Creegan, V. Srivastava, M. Jarzembski, and G. Fernandez, "Stimulated Raman scattering in micrometer-sized droplets: time-resolved measurements," Opt. Lett. **13,** 494–496 (1988).
7. W. F. Hsieh, J.-B. Zheng, and R. K. Chang, "Time dependence of multiorder stimulated Raman scattering from single droplets," Opt. Lett. **13,** 497–499 (1988).
8. Y. R. Shen, *The Principles of Nonlinear Optics* (Wiley, New York, 1984), pp. 141–201.
9. A. J. Campillo, J. D. Eversole, and H-B. Lin, "Cavity quantum elecrodynamic enhancement of stimulated emission in microdroplets," Phys. Rev. Lett. **67,** 437–440 (1991).
10. H. A. Haus, *Waves and Fields in Optoelectronics* (Prentice-Hall, Englewood Cliffs, N.J., 1984), pp. 201–202.
11. S. C. Hill and R. E. Benner, "Morphology-dependent resonances," in *Optical Effects Associated with Small Particles,* P. W. Barber and R. K. Chang, eds. (World Scientific, Singapore, 1988), pp. 3–61.
12. P. W. Barber and S. C. Hill, *Light Scattering by Particles* (World Scientific, Singapore, 1990), pp. 228–229.
13. D. S. Benincasa, P. W. Barber, J.-Z. Zhang, W.-F. Hsieh, and R. K. Chang, "Spatial distribution of the internal and near-field intensities of large cylindrical and spherical scatterers," Appl. Opt. **26,** 1348–1356 (1987).
14. A. Penzkofer, A. Laubereau, and W. Kaiser, "High intensity Raman interactions," J. Prog. Quantum Electron. **6,** 55–140 (1979).
15. D. von der Linde, M. Maier, and W. Kaiser, "Quantitative investigations of the stimulated Raman effect using subnanosecond pulses," Phys. Rev. **178,** 11–17 (1969).
16. Calculated from the measured values of the spontaneous Raman cross section and the linewidth of 5 M NH_4NO_3 dissolved in water.
17. G. M. Hale and M. R. Querry, "Optical constants of water in the 200-nm to 200-μm wavelength region," Appl. Opt. **12,** 555–563 (1973).
18. J.-Z. Zhang, D. H. Leach, and R. K. Chang, "Photon lifetime within a droplet: temporal determination of elastic and stimulated Raman scattering," Opt. Lett. **13,** 270–272 (1988).
19. R. Thurn and W. Kiefer, "Structural resonances observed in the Raman spectra of optically levitated liquid droplets," Appl. Opt. **24,** 1515–1519 (1985).
20. T. R. Lettieri and R. E. Preston, "Observation of sharp resonances in the spontaneous Raman spectrum of a single optically levitated microdroplet," Opt. Commun. **54,** 349–352, (1985).
21. J. B. Snow, S.-X. Qian, and R. K. Chang, "Stimulated Raman scattering from individual water and ethanol droplets at morphology-dependent resonances," Opt. Lett. **10,** 37–39 (1985).
22. H. Chew, "Radiation and lifetimes of atoms inside dielectric particles," Phys. Rev. A **38,** 3410–3416 (1990).
23. P. A. Fleury and R. Y. Chiao, "Dispersion of hypersonic waves in liquids," J. Acoust. Soc. Am. **39,** 751–752 (1966).
24. C. Hu and J. R. Whinnery, "New thermooptical measurement method and a comparison with other methods," Appl. Opt. **12,** 72–79 (1973).
25. J. Stone, "Measurement of absorption of light in low-loss liquids," J. Opt. Soc. Am. **62,** 327–333 (1972).
26. Assumed to be of the same order of magnitude as the water value.